Numerical Simulations of the Discharge and the Plasma-wave Interaction in a Helicon Plasma Thruster

IEPC-2022-498

Presented at the 37th International Electric Propulsion Conference
Massachusetts Institute of Technology, Cambridge, MA, USA
June 19-23, 2022

Pedro Jiménez[1], Jiewei Zhou, Pablo Fajardo, Mario Merino, and Eduardo Ahedo
Equipo de Propulsión Espacial y Plasmas (EP2), Universidad Carlos III de Madrid, 28911 Leganés, Spain

A self-consistent simulation of the plasma transport and electromagnetic fields for the helicon plasma thruster prototype HPT03 is presented. A hybrid particle-in-cell/fluid approach is employed for the slow plasma transport, while a full-wave frequency-domain finite element approach is used for the fast electromagnetic waves. Both aspects of the simulation are coupled in the limit of separate time scales. Results show that the magnetic ring cusp present in the plasma source determines the maps of plasma properties. The largest losses of the system are attributed to the wall losses inside the source, in the region where the magnetic cusp is located and magnetic lines are essentially perpendicular to the wall. The downstream electron-cyclotron resonance surface in the magnetic nozzle accounts for a large power deposition per particle, which rises the electron temperature on the magnetic lines disconnected from the source. [a]

I. Introduction

Helicon plasma thrusters (HPT) [1–4] are part of the electrodeless plasma thruster family, and consist of a cylindrical discharge chamber with a gas inlet, an inductor/antenna to supply RF power to ionize the propellant into a plasma and heat it, and an applied magnetic field, which aims to confine the plasma from the thruster walls and makes it transparent to the RF waves, and forms a magnetic nozzle outside of the device to accelerate it. The right-hand polarized whistler wave that propagates in the plasma in the parametric range of operation delivers power to the electrons by collisional, resonant, and/or kinetic damping.

The modeling and simulation of the plasma discharge in a thruster enables studying its physics, identifying dominant mechanisms, and eventually optimizing its design. Modeling the HPT is a complex task, as several interconnected processes must be modeled self-consistently. First, there is the magnetized plasma transport problem, which must also solve for ionization, the interaction with the walls and the external expansion and acceleration to infinity. Second, there is the plasma-wave interaction problem, coupled to the first as the fast wavefields are dependent on the plasma density and electron collisionality rate, and their power deposition drives the source term in the electron energy equation.

This work presents a coupled plasma transport/plasma wave model of the HPT device under development in the EU HIPATIA project. The focus of the study is on solving self-consistently the two problems stated above, finding the maps of the plasma properties together with the electromagnetic fields and power absorption density in a wide domain that includes the plasma source, the magnetic nozzle, and the peripheral region. We discuss how the magnetic cusp in the source affects the electron temperature map and induces a penalty in terms of wall losses, which has a major toll on the thruster performances. We then analyze the particle fluxes to each surface of the device to better characterize losses. Finally, we show that the existence of an electron-cyclotron resonant surface downstream in the plume accounts for a major power deposited per electron, which has an impact on the observed electron temperature.

The rest of the paper is structured as follows: Section II presents the plasma transport and plasma-wave interaction models employed for the numerical simulation of the device physics. Section III.A shows the setup parameters, the applied magnetic field and the different simulation domains. Detailed analysis of the solution plasma discharge profiles

[1]pejimene@ing.uc3m.es

and the electromagnetic wave propagation can be found in Sections III.B and III.C respectively. The device performance and losses are further discussed in Section III.D. Finally, some conclusions and future work are presented in Section IV.

II. Simulation Model

The plasma transport and the propagation of electromagnetic waves are intimately coupled, but each phenomenon can be modelled independently. The processes are later coupled together in a simulation loop that leverages the separation of time scales expected of each subproblem: most HPT designs feature antenna frequencies in the range of tens of MHz i.e. the characteristic time for wave induced field variations is on the order of 10^{-7} s. On the other hand, typical ion transit times in EPT are no less than 10^{-5} s. Consequently, the relevant plasma properties (density and temperature) appear static for a traveling electromagnetic wave and, conversely, the plasma ions only react to a cycle averaged effect induced by the fast fields. This separation strategy has been successfully used to analyze the slow plasma dynamics in the source on the one hand [5–8], and the internal electromagnetic field problem on the other hand [9–11].

Figure 1 shows the structure of the code and the interaction between its modules. We implement an ion(I)-module and an electron(E)-module solving for the slow transport of, respectively, the heavy species and electrons. In addition, there is a Sheath(S)-module solving for the Debye sheaths at the domain walls. These three modules constitute the, time marching, hybrid plasma transport solver. Finally, the W-module implements a finite element method solving the Maxwell equations for the waves in the frequency domain, and computes the power density map $P_a'''(\boldsymbol{r})$, needed for the plasma transport, taking as inputs the quasineutral plasma density n_e and an effective electron collision frequency ν_e. The simulation loop is run until convergence to a self-consistent stationary solution.

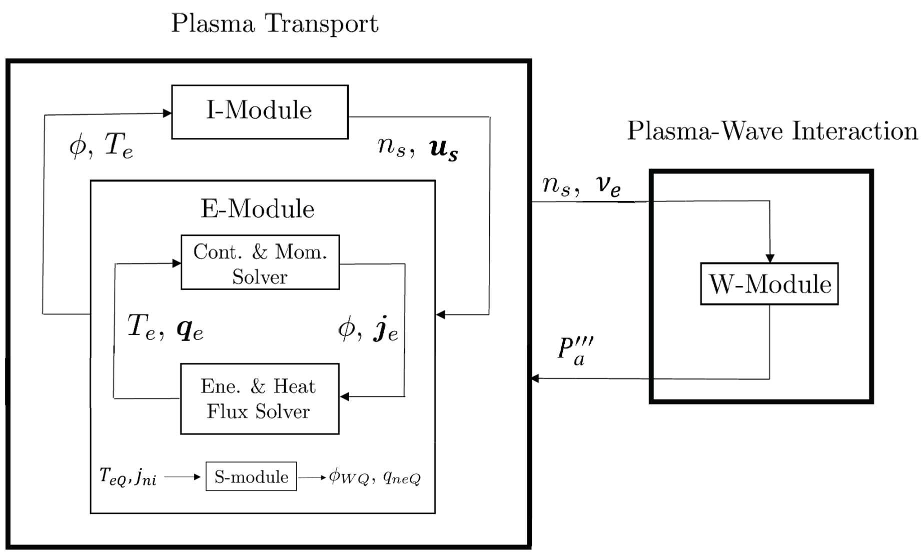

Fig. 1 Overall simulation model, modules and interfaces.

A. Hybrid model of plasma transport

The time marching transport solver is composed of two different modules that, in addition to the outer loop for the EM power, are also run sequentially. Heavy species (ions and neutrals) are modelled kinetically in the so called I-module. On the other hand, electrons are simulated with a fluid approach in the E-module. For a time step Δt of the heavy species, the electron fluid is advanced N_e times with a time step $\Delta t/N_e$. This allows for the electron fluid to reach a quasi-stationary solution each call. The coupling variables and interfaces are shown in Figure 1 and explained below.

The I-module implements the PIC model. The macro-particle populations are evolved in time according to the potential map that comes from the electron fluid solution and the applied magnetic field $\boldsymbol{B}$. Monte Carlo collisions are used to model the ionization and wall recombination events. The PIC model uses the Cartesian mesh of Figure 2, which is defined by $\{\mathbf{1}_z, \mathbf{1}_r, \mathbf{1}_\theta\}$, with coordinates (z, r, θ). The mesh is non-uniform and adapted to the expected plasma gradients and to keep a statistically acceptable number of macro-particles per cell.

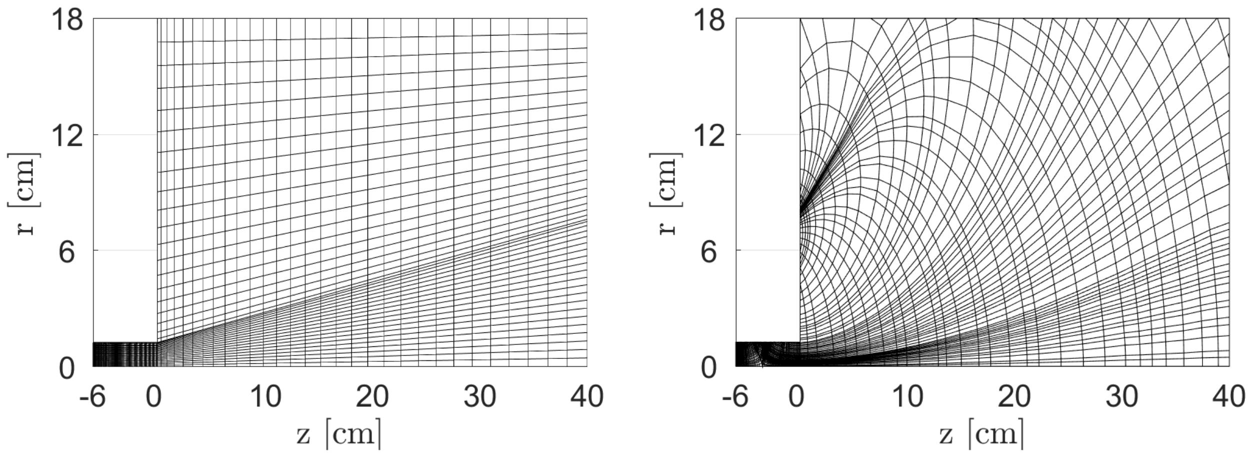

Fig. 2 Cartesian mesh (I-module) and Magnetic Field Aligned Mesh (MFAM) (E-module).

The E-module implements a weakly collisional, diffusive, magnetized, fluid model for electrons,

$$n_e = \sum_{s \neq e} Z_s n_s, \tag{1}$$

$$\nabla \cdot \boldsymbol{j}_e = -\nabla \cdot \boldsymbol{j}_i, \tag{2}$$

$$0 = -\nabla \left(n_e T_e\right) + e n_e \nabla \phi + \boldsymbol{j}_e \times \boldsymbol{B} + \boldsymbol{F}_{res} + \boldsymbol{F}_{ano}, \tag{3}$$

$$\frac{\partial}{\partial t}\left(\frac{3}{2} n_e T_e\right) + \nabla \cdot \left(\frac{5}{2} T_e n_e \boldsymbol{u}_e + \boldsymbol{q}_e\right) = -\nabla \phi \cdot \boldsymbol{j}_e + P_a''' - P_{\text{inel}}''', \tag{4}$$

$$0 = -\frac{5 n_e T_e}{2e} \nabla T_e - \boldsymbol{q}_e \times \boldsymbol{B} + \boldsymbol{Y}_{\text{res}} + \boldsymbol{Y}_{\text{ano}}, \tag{5}$$

where the unknowns are n_e, ϕ, $\boldsymbol{j_e}$, T_e and $\boldsymbol{q_e}$.

On account of previous studies showcasing an improved numerical behavior and reduced non-physical diffusion, the electron fluid equations are solved in the magnetically aligned mesh (MFAM) of Figure 2.b, defined by the applied magnetic field $\boldsymbol{B}_a$. The equations are projected accordingly using the vector basis $\{\mathbf{1}_\parallel, \mathbf{1}_\perp, \mathbf{1}_\theta\}$, where $\mathbf{1}_\perp = \mathbf{1}_\theta \times \mathbf{1}_\parallel$. The I-module provides the right hand side of Eqs.(1,2) imposing quasi-neutrality and conservation of the total current $\boldsymbol{j} = \boldsymbol{j_e} + \boldsymbol{j_i}$. Eq.(2) replaces consistently the more difficult to integrate electron continuity equation $\partial n_e / \partial t + \nabla \cdot n_e \boldsymbol{u}_e = S_e$, where the electron source term S_e is implicitly computed in the I-module for the production and recombination of both singly and doubly charged ions [12–14].

Beside the usual pressure and Lorentz forces, the momentum equation (3) implements an additional phenomenological force accounting for anomalous transport $\boldsymbol{F}_{ano}$ and the resistive force arising from electron collisions

$$\boldsymbol{F}_{res} = \left(m_e \nu_e / e\right)\left(\boldsymbol{j}_e + \boldsymbol{j}_c\right), \tag{6}$$

where $\nu_e = \sum_{s \neq e} \nu_{es}$ is the total electron effective collision frequency due to each heavy species $\nu_{es}(T_e)$; this includes the momentum transfer from elastic, ionization and excitation collisions with neutrals and Coulomb collisions and double ionization with ions. Finally, $\boldsymbol{j}_c = e n_e \sum_{s \neq e} \left(\nu_{es}/\nu_e\right) \boldsymbol{u}_s$ sets the contribution of each species s to the resistive force.

Evidence of anomalous transport in EPT thrusters is still limited [15], but expected from the devices' configuration. In the present work, the phenomenological models derived and long applied to the study of Hall effect thrusters [16, 17] are applied to the HPT. The anomalous force term reads:

$$\boldsymbol{F}_{ano} = \alpha_{ano} B j_{\theta e} \mathbf{1}_\theta, \tag{7}$$

where α_{ano} is a fitting parameter. The net effect of this force is an increased in the perpendicular transport of electrons. Eq.(4) is the energy equation. The variation of internal energy comes from the convective plus conductive fluxes, the work of the electric field $-\nabla\phi \cdot \boldsymbol{j_e}$ and two source terms. The first one, P_a''' is the volumetric power density deposited by the electromagnetic fields, this term is computed by the W-module and kept constant between wave solver calls. The second term is the power lost by electrons during inelastic collisions,

$$P_{inel}''' = n_e \sum_{s\neq e} \nu_{es,inel}\varepsilon_{es} \tag{8}$$

where ε_{es} is the energy threshold for ionization or excitation. The system is closed at the heat flux equation (5). Analogous to the also drift-diffusive momentum equation (3), this expression includes a resistive term

$$\boldsymbol{Y}_{res} = -\left(m_e\nu_e/e\right)\boldsymbol{q}_e \tag{9}$$

and the doubly-anomalous term

$$\boldsymbol{Y}_{\text{ano}} = -\alpha_{\text{ano}} B q_{\theta e}\mathbf{1}_\theta - \left(m_e\nu_q/e\right) q_{\parallel e}\mathbf{1}_\parallel. \tag{10}$$

The new phenomenological parameter ν_q was added recently [14] to limit the parallel conductivity of the electron fluid. This helps reproduce observed physical phenomena like downstream electron cooling in the near-collisionless plume. The drift-diffusive equations (3,5) provide the so called Generalized Ohm's and Fourier's laws.

The boundaries of the quasineutral domain are closed with the S-module, which, provided the electron temperature T_e and ion species currents at the sheath edge, fixes the necessary electron current and heat fluxes and the sheath potential fall ϕ_{WQ} between the quasinuetral boundary point Q and the wall W. The S-module accounts for material type, recombination and secondary electron emission by providing different plasma-wall interaction models and fitting parameters. For the simulations presented in this work we use a dielectric wall BC i.e. $\boldsymbol{j_e} + \boldsymbol{j_i} = 0$ accounting for the ceramic walls in the plasma source. For the downstream free loss surfaces, the model of the global downstream matching layer is implemented, which imposes a floating condition, $\iint_{FL} \boldsymbol{j}\cdot\boldsymbol{n}\mathrm{d}S = 0$, through a potential at the infinity (out of the simulation domain), in substitution to the local ambipolarity condition used before. See [14, 18] for further references.

The numerical integration of the system is based on a semi-implicit scheme for the time discretization and finite volume/gradient reconstruction methods for the spatial discretization [8, 14].

B. Electromagnetic wave model

The wave fields are solved using a full-wave Finite Element method in the Frequency Domain (FEFD). The electromagnetic model presented in this work follows the general structure of [19] but includes a novel feature to simulate propagation at arbitrary azimuthal mode numbers $m \neq 0$ [20]. This is is essential for the modelling of Helical antennas in HPTs and was previously applied to EPTs and plasma source simulations with Finite Difference (FD) discretizations [10, 11, 21].

In order to find the steady state EM fields with a given antenna excitation frequency ω, we expressed any time harmonic field $\mathcal{F}$ as

$$\mathcal{F}(\boldsymbol{r}, t) = \Re\left[\hat{\boldsymbol{F}}(\boldsymbol{r})\exp(-\mathrm{i}\omega t)\right], \tag{11}$$

Faraday's and Ampere's laws for the electric field $\hat{\boldsymbol{E}}$ and magnetic field $\hat{\boldsymbol{B}}$ amplitudes in frequency domain are

$$\nabla\times\hat{\boldsymbol{E}} = \mathrm{i}\omega\hat{\boldsymbol{B}} \tag{12}$$

$$\nabla\times\hat{\boldsymbol{B}} = -\mathrm{i}\omega\mu_0\hat{\boldsymbol{D}} + \mu_0\hat{\boldsymbol{J}}_a \tag{13}$$

where $\hat{\boldsymbol{J}}_a$ is the amplitude of the applied antenna current density, μ_0 is the vacuum permeability constant and ε_0 (used later) is vacuum's permittivity. These two equations automatically impose $\nabla\cdot\hat{\boldsymbol{B}} = 0$ and $\nabla\cdot\hat{\boldsymbol{D}} = -i\nabla\cdot\hat{\boldsymbol{J}}_a/\omega = 0$, for any charge conserving applied current i.e. $\nabla\cdot\hat{\boldsymbol{J}}_a = 0$. By virtue of the cold plasma assumption, the magnetized plasma response can be modelled linearly using an anisotropic dielectric tensor $\overline{\overline{\kappa}}$. The electric displacement field becomes

$$\hat{\boldsymbol{D}} = \varepsilon_0\overline{\overline{\kappa}}\cdot\hat{\boldsymbol{E}} \tag{14}$$

In what follows we will ignore the slow response of ions and write the components of $\overline{\overline{\kappa}}$ in the magnetically aligned vector basis $\{\mathbf{1}_\parallel, \mathbf{1}_\perp, \mathbf{1}_\theta\}$ [22],

$$\overline{\overline{\kappa}}(z, r) = \begin{pmatrix} P & 0 & 0 \\ 0 & (R+L)/2 & -i(R-L)/2 \\ 0 & i(R-L)/2 & (R+L)/2 \end{pmatrix}, \tag{15}$$

with

$$R = 1 - \frac{\omega_{pe}^2}{\omega(\omega + \mathrm{i}\nu_e - \omega_{ce})}, \qquad L = 1 - \frac{\omega_{pe}^2}{\omega(\omega + \mathrm{i}\nu_e + \omega_{ce})}, \qquad P = 1 - \frac{\omega_{pe}^2}{\omega(\omega + \mathrm{i}\nu_e)};$$

where the electron cyclotron and plasma frequencies are defined as

$$\omega_{ce}(z,r) = \frac{eB_a}{m_e}, \qquad \omega_{pe}(z,r) = \sqrt{\frac{ne^2}{m_e\varepsilon_0}}; \tag{16}$$

and the rest of symbols are conventional. The electron cyclotron and plasma frequencies, $\omega_{ce} \propto B_a$ and $\omega_{pe} \propto n^{-1/2}$, are the main plasma parameters in the electromagnetic model, while the electron collisionality, ν_e, is secondary as long as $\nu_e/\omega \ll 1$. The tensor $\overline{\overline{\kappa}}$ is rotated to the cylindrical vector basis used in the problem discretization.

Taking the divergence of (12) and substituting into (13) we eliminate $\hat{B}$, obtaining the second order wave equation for $\hat{E}$:

$$\nabla \times (\nabla \times \hat{\boldsymbol{E}}) - k_0^2 \overline{\overline{\kappa}} \cdot \hat{\boldsymbol{E}} = i\omega\mu_0 \hat{\boldsymbol{J}}_{\boldsymbol{a}}, \tag{17}$$

where we have introduced the vacuum wave number $k_0 = \omega\sqrt{\varepsilon_0\mu_0}$.

Next, we perform the Fourier decomposition in θ of the fields, so that $\hat{\boldsymbol{F}}(z,r,\theta)$ can be express as a superposition of its modes,

$$\hat{\boldsymbol{F}}(z,r,\theta) = \sum_{m=-\infty}^{\infty} \boldsymbol{F}^{(m)}(z,r)\exp(\mathrm{i}m\theta) : \qquad \boldsymbol{\mathcal{F}}(z,r,\theta,t) = \Re\left[\sum_{m=-\infty}^{\infty} \boldsymbol{F}^{(m)}(z,r)\exp(-\mathrm{i}\omega t + \mathrm{i}m\theta)\right]. \tag{18}$$

Above, m is the integer azimuthal mode number and $\boldsymbol{F}^{(m)}(z,r)$ is the complex magnitude vector at $t = 0$, $\theta = 0$ for mode m. These complex magnitudes for each m are the unknowns of the model. In the absence of impedance/resistive surfaces and introducing the Fourier expansion in azimuthal modes, we find the following weak form of (17),

$$\begin{aligned} &\iint_\Omega \left\{\left[\left(\nabla_t + \mathbf{1}_{\boldsymbol{\theta}}\frac{im}{r}\right)\times \mathbf{T}^{(m)}\right]\cdot\left[\left(\nabla_t - \mathbf{1}_{\boldsymbol{\theta}}\frac{im}{r}\right)\times \mathbf{E}^{(m)}\right] - k_0^2\mathbf{T}^{(m)}\cdot\overline{\overline{\kappa}}\cdot\mathbf{E}^{(m)}\right\} dS + \\ &+ ik_0\int_{\delta\Omega}\left[\hat{n}\times\mathbf{T}^{(m)}\right]\cdot\left[\hat{n}\times\mathbf{E}^{(m)}\right] dl = i\mu_0\omega\iint_\Omega \mathbf{T}^{(m)}\cdot\boldsymbol{J}_{\boldsymbol{a}}^{(m)} ds \end{aligned} \tag{19}$$

where Ω and $\delta\Omega$ are the simulation domain and its enclosing boundary and $\boldsymbol{T}^{(m)}$ is the test function. A mixed element discretization is used. The tangential fields (E_z and E_r) are projected in a edge-based vector basis (Nédélec elements) $\boldsymbol{N}_j$. The out-of-plane component E_θ is projected in standard nodal (Lagrange) scalar elements L_j [19]. For first order N_j and L_j, this yields

$$\mathbf{E}^{(m)} = \begin{cases} \sum_{j=1}^{N_{\text{edge}}} \mathbf{N}_j(r,z)e_{t,j}^{(m)} + \mathbf{1}_{\boldsymbol{\theta}}\sum_{j=1}^{N_{\text{node}}} L_j(r,z)e_{\theta,j}^{(m)} & m = 0 \\ \sum_{j=1}^{N_{\text{edge}}} r\mathbf{N}_j(r,z)e_{t,j}^{(m)} + (\mathbf{1}_{\boldsymbol{\theta}} \mp i\mathbf{1}_{\boldsymbol{r}})\sum_{j=1}^{N_{\text{node}}} L_j(r,z)e_{\theta,j}^{(m)} & m = \pm 1 \\ \sum_{j=1}^{N_{\text{edge}}} r\mathbf{N}_j(r,z)e_{t,j}^{(m)} + \mathbf{1}_{\boldsymbol{\theta}}\sum_{j=1}^{N_{\text{node}}} L_j(r,z)e_{\theta,j}^{(m)} & |m| > 1 \end{cases} \tag{20}$$

where $e_t^{(m)}$ and $e_\theta^{(m)}$ are the unknown expansion coefficients. Our code retains the capability of using higher-order elements. The conforming mixed element approach has proven successful in keeping the displacement field $\hat{\boldsymbol{D}}$ divergence-less and thus preventing the artificial accumulation of spurious current [23, 24]. The discretization in (20) implicitly applies the axial symmetry conditions for the tangential fields.

Boundary conditions are defined as follows. The regularity/smoothness [11] conditions at the symmetry axis are

$$\begin{aligned} &E_r^m = E_\theta^m = 0, && \text{for } m = 0, \\ &E_r^m = \mp iE_\theta^m, \quad E_z^m = 0, && \text{for } m = \pm 1, \\ &E_r^m = E_\theta^m = E_z^m = 0, && \text{for } |m| > 1 \end{aligned}$$

Additionally, the lateral and top walls of the rectangular domain are modelled as Perfect Electric Conductors (PEC). PEC boundaries are characterized by a null tangential electric field $\boldsymbol{E} \times \mathbf{1}_n = 0$. This condition is easily implemented setting to 0 some of the edge coefficients in (20). Future work must implement other boundary conditions and/or absorbing layers and assess their influence in the simulation results. The plasma current density induced by the wave electric field is:

$$\boldsymbol{J}_p^m = \mathrm{i}\omega\epsilon_0(\bar{\bar{1}} - \bar{\bar{\kappa}}) \cdot \boldsymbol{E}^m, \tag{21}$$

where $\bar{\bar{1}}$ is the identity tensor and the time-averaged power density deposited into the plasma by mode m is $P^{'''(m)} = \Re\left((\boldsymbol{J}_p^m)^* \cdot \boldsymbol{E^m}/2\right)$. The total resistive power seen at the antenna can be computed as the sum of the volume integral over the simulation domain for all the azimuthal modes,

$$P_a = \sum_m P_a^m, \qquad P_a^m = \int_\Omega P^{'''(m)} \mathrm{d}S. \tag{22}$$

The FEM discretization allows for the use of unstructured and adaptable meshes (not shown here due to the high density of nodes required to resolve very short wave-length structures). A triangular mesh is used, and it is possible to apply a refinement strategy such as the one outlined in [19] to account for shorter wavelengths and critical transitions. In general, the local mesh size is selected so that the number of nodes per wavelength is at least $N_\lambda > 20$. This is satisfied anywhere but near the ECR and the $P = 0$ surfaces (if the later exists in the simulation domain).

Finally, we mention for completeness the modelling of the current density associated to 3D Helical antennas, developed in the past and found in the literature under several complementary forms [11, 21, 25, 26]. We take an infinitely thin wire in the $z - \theta$ plane extending axially from $z_1 = z_a - l_a/2$ to $z_2 = z_a + l_a/2$, being z_a the central position of the antenna and l_a the length. Defining the helicity number h as the total number of turns of the antenna along the cylindrical tube, the axial component of the current density vector follows

$$\mathcal{J}_{za}(z, r, \theta) \propto \left\{\delta\left(\theta - \frac{2\pi h}{l_a}(z - z_1)\right) - \delta\left(\theta - \pi - \frac{2\pi h}{l_a}(z - z_1)\right)\right\} H(z - z_1)H(z_2 - z)G(r), \tag{23}$$

which represents the two wires of the antenna winding around the source. Above, δ is Dirac's Delta function, H is the Heaviside step function, and $G(r)$ is an smoothing function in r. Normally a Gaussian shape with a characteristic antenna thickness d_t is used, $G(r) = \exp(-(r - r_a)^2/d_t^2)$, where r_a is the radius of the antenna. There is freedom to choose any proportionality constant such that the surface integral of the current density on the wire cross-section can be set to any desired antenna current I_a. The radial component of the current density vector is always zero for the helical antenna family $\mathcal{J}_{ra} = 0$. The azimuthal component can then be found by charge continuity $\nabla \cdot \mathcal{J}_a = 0$. Afterwards, the current density is decomposed into its Fourier modes obtaining the corresponding $\boldsymbol{J_a}^{(m)}(z, r)$ components.

Because of the orthogonality of the Fourier modes, the analysis can then be carried out independently for each of them. Previous studies on HPTs using Helical antennas have proven the prevalence of $m = 1$ in the total plasma resistivity [8, 27, 28]. Consequently, in this work, only the $m = 1$ mode will be considered and simulated.

III. Results and Discussion

A. Simulation Setup

A device similar to the HPT03 thruster developed jointly by SENER Aeroespacial and the EP2 lab at Universidad Carlos III will be studied [29]. This is a compact (300-500W) Helicon Plasma Thruster with a 1.25 cm source radius and 6 cm source length. The magnetic field is generated by an annular magnet creating the topology shown in Figure 4. The magnetic topology of the HPT03 includes a cusp ring inside the source. The singular (0 magnitude) magnetic field point is located at $z = -3.5$ cm on the symmetry axis. The magnets create a radial field at this axial location before becoming almost axial at the thruster exit. As discussed later, this non-conventional topology is relevant to the magnetic confinement of the plasma inside the device.

A novel feature in our present study is that we simulate past the ECR surface that exists downstream in the plume region, where the strength of the magnetic field is low enough to match the resonance condition. This is achieved by extending the plume domain further downstream than previous works in HPTs [30]. The resonance surface is displayed as a green line in Figure 4a. The neutral propellant, monatomic Xenon, is injected through the backwall wall of the plasma source at a 1 mg/s rate. An helical antenna is used for the heating of the plasma inside the vessel. The geometric and operational parameters are displayed in Table 1.

The dimensions of the different sub-domains are shown in Figure 3. The wave domain (blue) encloses the HYPHEN transport domain (red for source and yellow for plume). Besides the injector surface, the source walls are dielectric

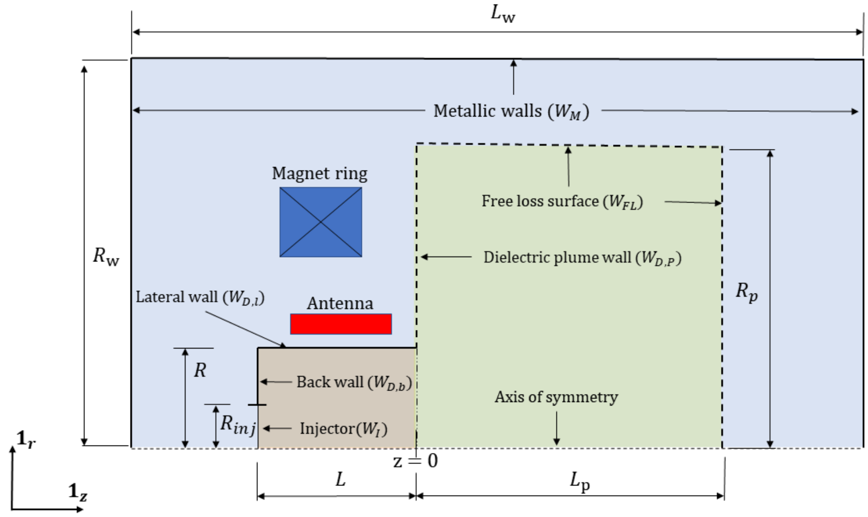

Fig. 3 Simulation domain and boundary conditions (not to scale). The red (source) and yellow (plume) areas comprise the transport domain. The larger wave domain is depicted in blue.

while a free loss surface is set in the plume region. The boundaries of the wave domain are metallic walls modelling the laboratory vacuum chamber. Despite being placed excessively close to the thruster for a realistic setup, we show that almost no electromagnetic radiation reaches the external boundaries due to the presence of the ECR surface downstream, and consequently, wave reflection at the chamber at those walls is deemed small.

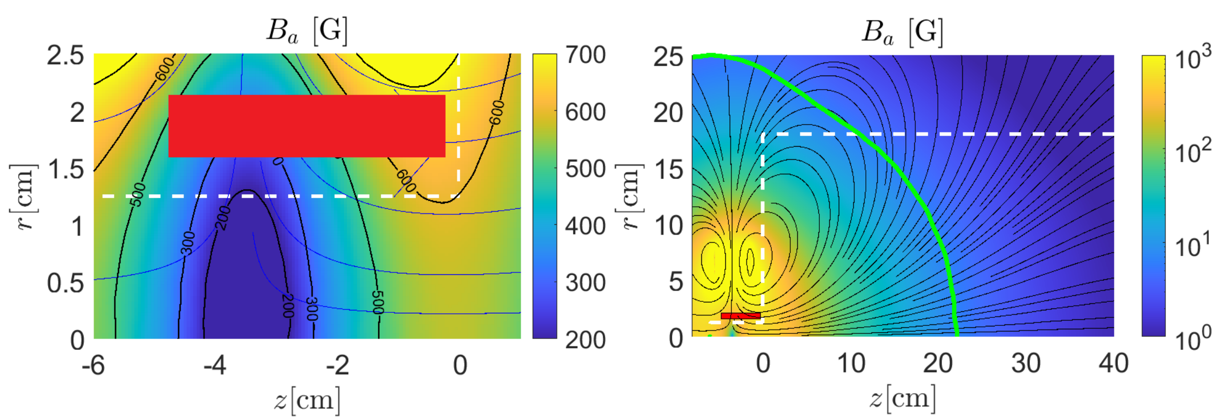

Fig. 4 Applied Magnetic Field. Zoom at the source region (left) and full wave domain (right). The antenna is depicted in red and the boundary of the transport domain by a white dashed line.

The wave mesh is noticeably finer than the PIC and MFAM meshes in order to resolve accurately short wave lengths appearing in certain low density regions and transitions. While these wavelengths are smoothed out when P_a''' is interpolated to the coarser meshes, not resolving them would result in numerical noise propagating to the rest of the domain [11].

Following [14] the simulation is pre-initialized by calling the I-module alone, with a Boltzmann relation-like model for the electrostatic potential. This allows for the simulation domain to be quickly filled with macro-particles coming from the injector before calling the electron and wave modules. The selection of N_w is based on an educated guess and previous numerical studies on the plasma dynamics and is normally a compromise between very frequent EM calls, slowing down the simulation, and undesired oscillations for large N_w that might hinder a fast convergence.

Simulation Parameter	Symbol	Units	Value
Thruster length	L	cm	6
Thruster radius	R	cm	1.25
Injector radius	R_{inj}	cm	0.625
Neutral gas mass flow	$\dot{m}$	mg/s	1.72
Heavy species	-	-	Xe, Xe^{+}, Xe^{2+}
Anomalous transport coefficient	α_{ano}	-	0.03
Anomalous cooling collisionality	ν_q	-	0.0
Plume length	L_p	cm	40
Maximum plume radius	R_p	cm	18
I-mesh size	-	cells	4961
E-mesh size	-	cells	3671
I-module time step	Δt	s	$2.5 \cdot 10^{-8}$
E-module time step sub-iterations	N_e	-	5
Total simulation time	t_{sim}	ms	3.75
Rectangular wave mesh	-	cm	$z \in [-13.5, 43]$, $r \in [0, 25]$
W-mesh size	-	cells	10^6
W-module call frequency	$1/N_w$	-	1/50
Antenna type	-	-	Half-turn Helical, $h = 0.5$
Antenna frequency	$f = \omega/(2\pi)$	MHz	13.56
Antenna Power	P_a	W	500
Antenna loop radius	r_a	cm	1.85
Antenna length	l_a	cm	4.5
Antenna central position	z_a	cm	3.5
Antenna thickness	d_t	cm	0.5

Table 1 Nominal Simulation Parameters.

Compared to previous coupled EPT simulations [19], the larger domain (both radially and axially) and the magnetic topology, push the limits of the model and impose more restrictive simulation settings. The wave solver is called about 100 times more frequently to avoid numerical oscillations. The wave mesh has about 10 times the number of cells, while the PIC cells are almost doubled. In order to achieve a statistically sufficient number of particles per cell in the plume periphery, the number of mean particles per cell had to be increased threefold at steady state, reaching 1000 at some cells in the source in spite of population control strategies.

Steady state (both in the thrust and efficiency figures) is achieved after 3.75 ms of physical time. Minor oscillations around a central value can be still observed at the plume periphery but they are found to be irrelevant for the solution in the rest of the simulation domain. Customary to PIC simulations, the results in the next section are time-averaged over 200 I-module steps to filter noise and short period oscillations.

B. 2D Plasma Discharge Profiles

This section presents the different 2D plasma profiles obtained in the coupled simulations. It is convenient to express any 3D vector field as the sum of its longitudinal vector component plus the out of plane contribution. We will denote the former with a tilde such that, for any vector field $\boldsymbol{F}$, it is $\boldsymbol{F} = \tilde{\boldsymbol{F}} + F_\theta \mathbf{1}_\theta$. Characteristic values/ranges of plasma conditions found in the simulation domain are displayed in Table 2.

The neutral density is shown in the first row of Figure 5 (full domain right, zoom view of the source left). Neutral density n_n reaches its maximum at the injector surface and the decrease is essentially axial along the source region. This profile results from the balance between neutral consumption due to ionization, and neutral recombination where ions impinge on the wall. In the almost collisionless plume, the density fall is driven solely by the gas expansion.

Regarding the plasma density (2nd row Figure 5), it is observed that the maximum is located at the axis and near the magnetic singular point ($z = -3.5$ cm) peaking slightly below $n_e = 10^{20}$ m^{-3}. Consistent with wall recombination, the

Variable	Symbol	Units	Value
Applied Magnetic Field	B_a	G	10^0-10^3
Gyro-frequency	ω_{ce}	s^{-1}	10^7-10^{10}
Density	n_e	$1/m^3$	10^{15}-10^{20}
Debye Length	λ_D	m	10^{-6}-10^{-3}
Temperature	T_e	eV	2-6
Effective Collision Frequency	ν_e	s^{-1}	10^4-10^8

Table 2 Characteristic plasma conditions in the simulation domain.

density decreases toward the back and lateral walls. The plasma acceleration becomes evident toward the exit of the source and at the expansion at the plume.

The electron temperature map inside the source, ranging in T_e = 2-5 eV (Figure 5), is much affected by the topology of the applied magnetic field. Indeed, (1) the behavior along magnetic lines is near-isothermal, as the magnetic field hinders the perpendicular particle and heat transport, (2) the cusp divides the source into two regions, left with lower T_e, and right with milder T_e, and (3) the maximum T_e in the source is considerably low (lower than devices with standard axial magnetic topologies [14]). As discussed further on, this is due to the large particle and power loss to the walls in the cusp region, where magnetic lines are essentially perpendicular to the lateral wall. Remarkably, our parametric studies show that the T_e solution is only weakly affected by the anomalous transport coefficient α_{ano}, whereas in other devices it is known to have an important impact on the temperature profiles.

The map of T_e in the plume also merits discussion. Electron temperature continues to be quasi-isothermal in the MN; this is confronted to some experimental results [31, 32] and kinetic models [33, 34] that show some degree of parallel cooling. This is partly due to the large parallel heat conduction in the essentially-collisionless expansion, but also, it is affected by the power deposition at the downstream ECR surface, as discussed further on. Electron cooling is expected to occur further downstream of this ECR surface [10].

The power deposition at the ECR surface also accounts for the peak value of T_e taking place in the peripheral plume. Indeed, in absence of significant perpendicular transport and conduction, the temperature along a magnetic line only depends on the integrated effect of power sources and sinks along that line. The larger power deposition per electron (later shown in Figure 10) in the thin ECR surface defines this balance and rises the temperature in these magnetic lines. Despite the increase in temperature, the electron pressure p_e remains low as does the plasma density.

The electrostatic potential map (bottom row Figure 5) illustrates the gradient at the source exit and plume leads to an axial electric field that accelerates ions downstream. Contrary to other magnetic setups, where the maximum of ϕ is located near the rear wall, in this case the maximum is located at the position of the magnetic cusp. Along any magnetic line i.e. $\mathbf{1}_{\parallel}$ and in the absence of collisional processes i.e at the plume region, the plasma density, potential and temperature can be recognized to follow approximately the Boltzmann relation

$$\frac{n_e}{n_{e0}} \simeq \exp \frac{e\left(\phi - \phi_0\right)}{T_e}. \tag{24}$$

The potential drop toward the rear and lateral walls contributes to the high ion flux to the dielectrics.

Figure 6 shows the electron (top) and ion (bottom) in-plane current densities. Arrows indicate the streamlines of each species, independently of their charge sign. The current density maps in the source are indicative that there is a very significant particle flux to the back and lateral walls, with streamlines (in particular, electron's) reproducing the shape of the cusped magnetic field. Moreover, very few ions are capable of crossing the separatrix. This result is remarkable considering that ions are only weakly magnetized, i.e. the ion motion is governed mainly by the electric field. The ion production to the left of the singular point is therefore almost completely lost to the dielectric walls.

In the plume, ions present a conventional acceleration profile following the electic potential drop. On the other hand, while the global current ambipolarity conditions imposed at the boundary are less restrictive than the local ones, electron lines show partial closure downstream, with lines almost parallel to the right boundary. The flux of ions and electrons to the peripheral region is small due to the magnetic isolation of this area.

Figure 7 shows the integrated electron and ion fluxes to the boundaries of the domain. The global current condition is exemplified at the top and right plume boundaries where the local electron and ion currents don't match locally (the dielectric walls impose this condition by definition). Figure 7 (right) evidences that the maximum current is reached just

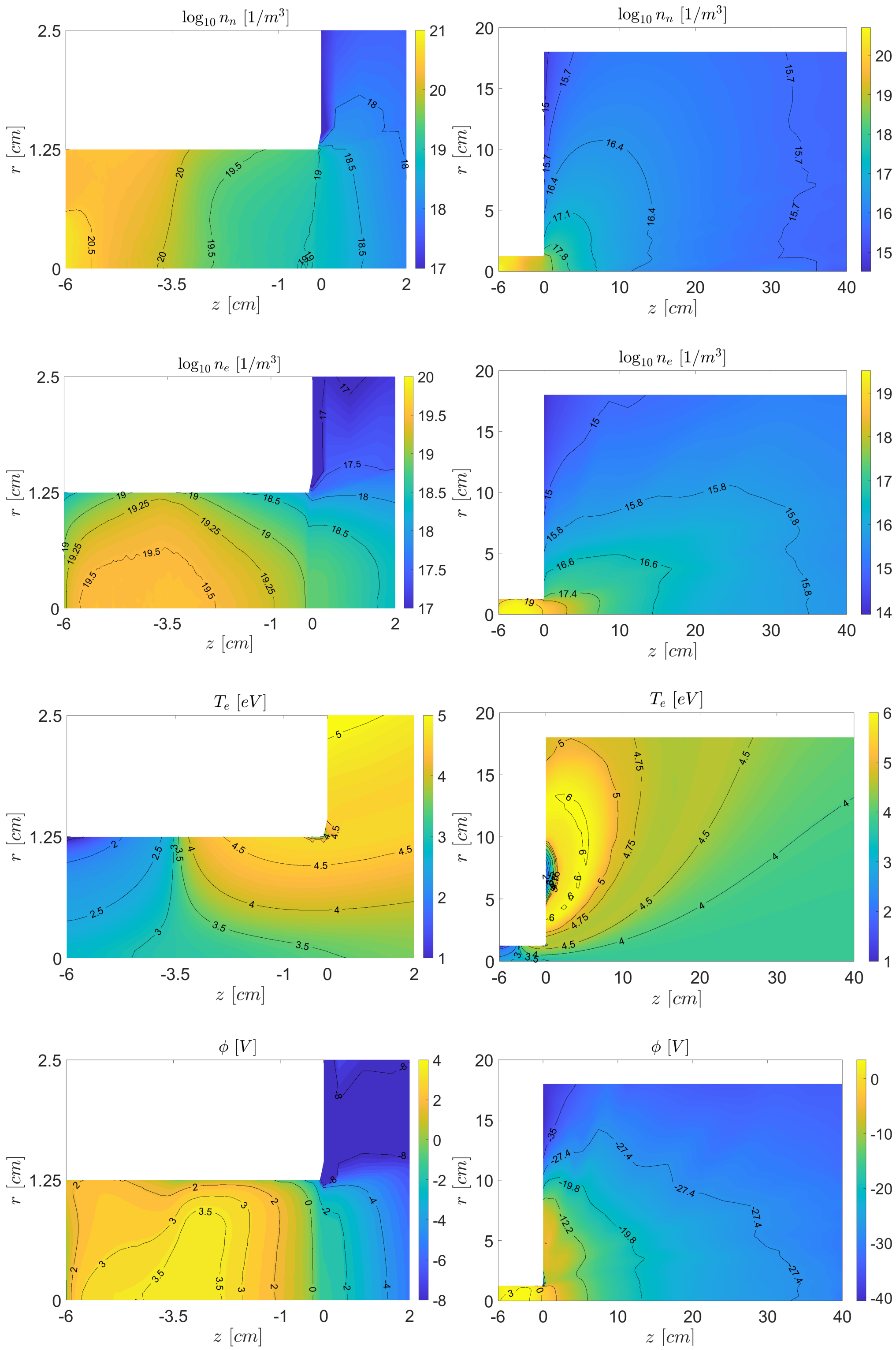

Fig. 5 Neutral (1st row) density, plasma density (2nd row), electron temperature (3rd row) and plasma potential (4th row). Zoom at the source region (left column) and full transport domain view (right column).

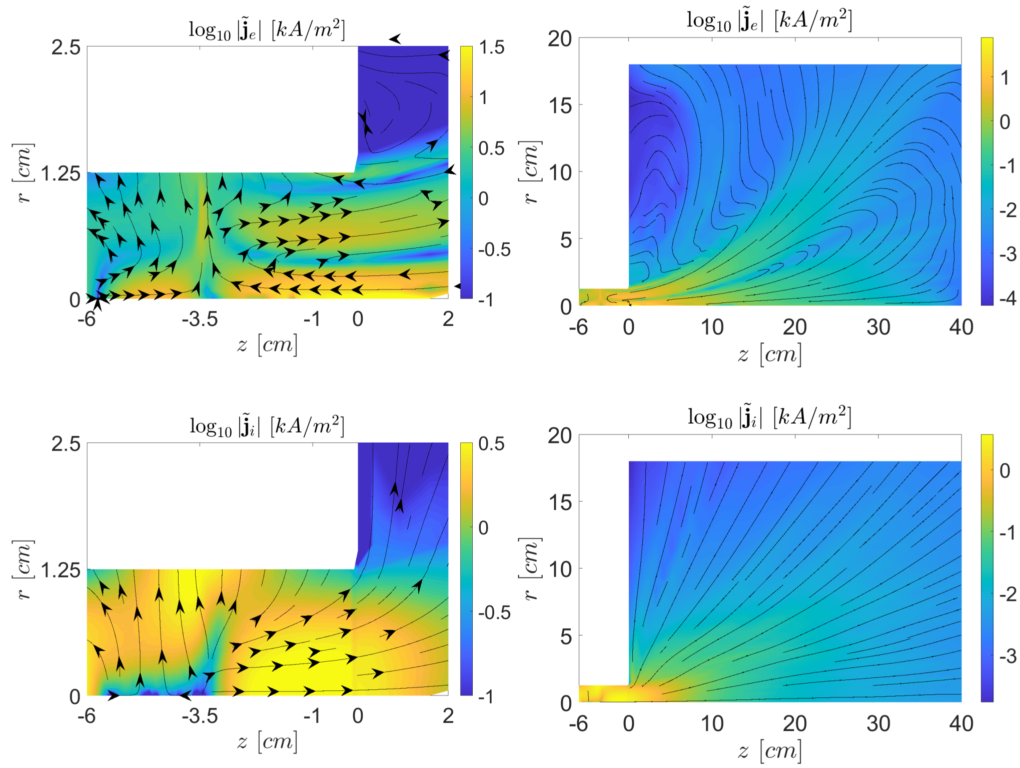

Fig. 6 Electron (top row) and ion (bottom) current densities. Zoom at the source (left) and full transport domain (right).

at $z = -3.5$ cm, demonstrating not only the poor confinement in the source, but that the applied magnetic field drives the particles directly into the walls.

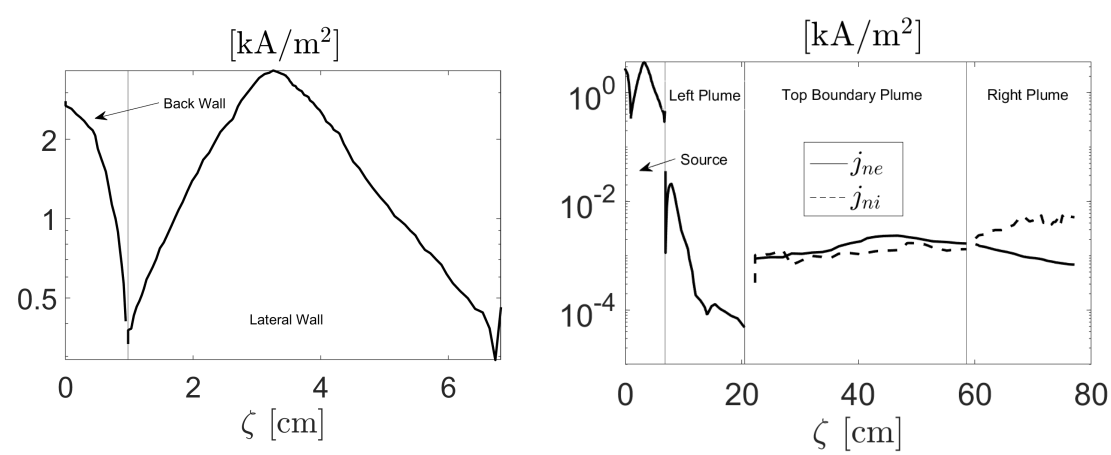

Fig. 7 Electron and ion normal boundary current densities. Zoom at the source dielectric walls (left) and full transport domain boundaries (right).

The electron azimuthal current density $j_{\theta e}$ in the vessel region is shown in Figure 8. Considering the near-unmagnetized ions, the electron contribution constitutes the bulk of plasma azimuthal current. From the momentum equation (3), both the resultant electric field and the pressure gradient drift (i.e. diamagnetic drift) add to this current.

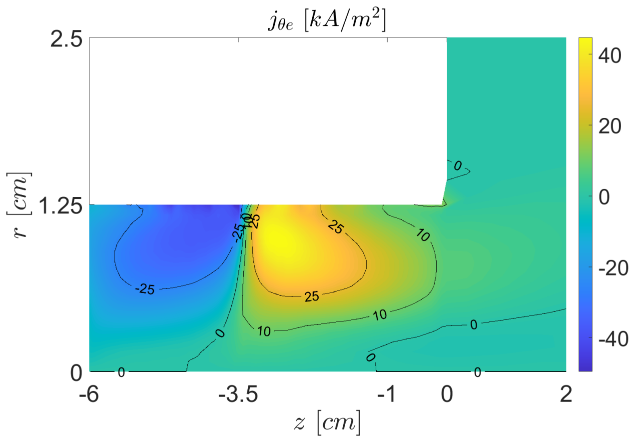

Fig. 8 Azimuthal electron current inside the source.

The net current is diamagnetic and therefore produces a radially-confining and axially-accelerating reaction force on the plasma. The reaction felt on the magnetic circuit is the magnetic thrust force. Again, the cusp plays a very relevant role, with the change of sign of the azimuthal current upon crossing the separatrix line being evident in Figure 8.

C. Wave-Plasma Interaction and Electromagnetic Power Deposition

We now turn our attention to the magnitude and phase of the self-consistent wave azimuthal electric field for the mode $m = 1$, shown in Figure 9. The fast field is strongest inside the source, decaying both in the plume and thruster surroundings and suggesting a good coupling between the RF antenna and the dense plasma. Despite the lower magnitude, the phase plot reveals propagation at the plume up to the ECR surface. Beyond it, the fields become evanescent [11, 22].

Our simulation setup imposes full vacuum outside the transport domain (white dashed line in Figure 8). This approximation is realistic considering the low densities at the transport domain boundaries (approaching the under-dense limit $\omega > \omega_{pe}$). It also avoids numerical noise and aliasing of very short waves that appear when the plasma density is very close to the critical value ($n_{e,c} \approx 10^{12}\mathrm{m}^{-3}$, this is of course a function of the antenna frequency). The fields in the surroundings are at least 2 orders of magnitude weaker than the ones anywhere at the plume. The vacuum wavelength for the operation frequency is about 30 m. Compared to previous work reporting numerical difficulties to solve the under-dense to over-dense transition ($P = 0$, or $\omega = \omega_{pe}$) [10], the FEM solver can solve this transition with less numerical noise. The successful resolution can also be attributed to the alignment of the mesh with the transitions (rectangular domains in the present simulation).

Along the axis, a low $k_\parallel$ helicon mode is seen to propagate in the source and near plume. The plume periphery presents shorter wavelengths consistent with the low, though over-dense, plasma density found there and the so-called Trivelpiece-Gould waves expected in this region [35]. These structures follow closely the magnetic field lines exhibiting a high perpendicular wave number $k_\perp$ unlike the almost-parallel propagation detected near the axis (moderate $k_\parallel$). Both kinds of waves (helicon and Trivelpiece-Gould) correspond to the right-hand polarized (R) whistler wave at different propagation angles, and both vanish upon arriving at the ECR surface. At this location, the electromagnetic power they carry can be either absorbed or reflected back in the vicinity of the resonance, but with the present plasma parameters, cannot propagate beyond. As a side note, we mention that there is another ECR surface in this simulation setup in the neighborhood of the singular point inside the plasma vessel. However, its effects are minor due to the limited spatial extent of that transition.

The power absorption profile is shown in the top row of Figure 10. Due to the linearity of the wave problem these maps can be also interpreted as the local plasma resistivity. Most of the power is absorbed within the source. This agrees well with plasma wave theory predicting an absorption approximately proportional to the plasma density for similar magnitude propagating fields. In the zoomed view of the source, we see that the maximum deposition is not located on the axis but displaced toward the lateral wall, along the separatrix and its vicinity.

Finally, the bottom row of Figure 10 displays the power absorbed *per electron*. The physical relevance of this quantity lies in the electron energy balance on each magnetic line, in as much as it provides the description of the local

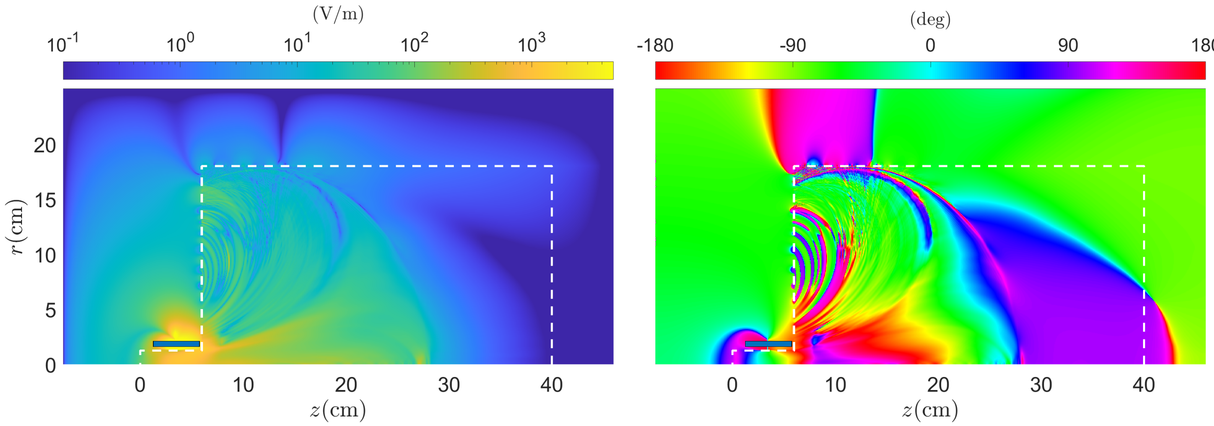

Fig. 9 E_θ^1 **field magnitude (left) and phase angle (right)**

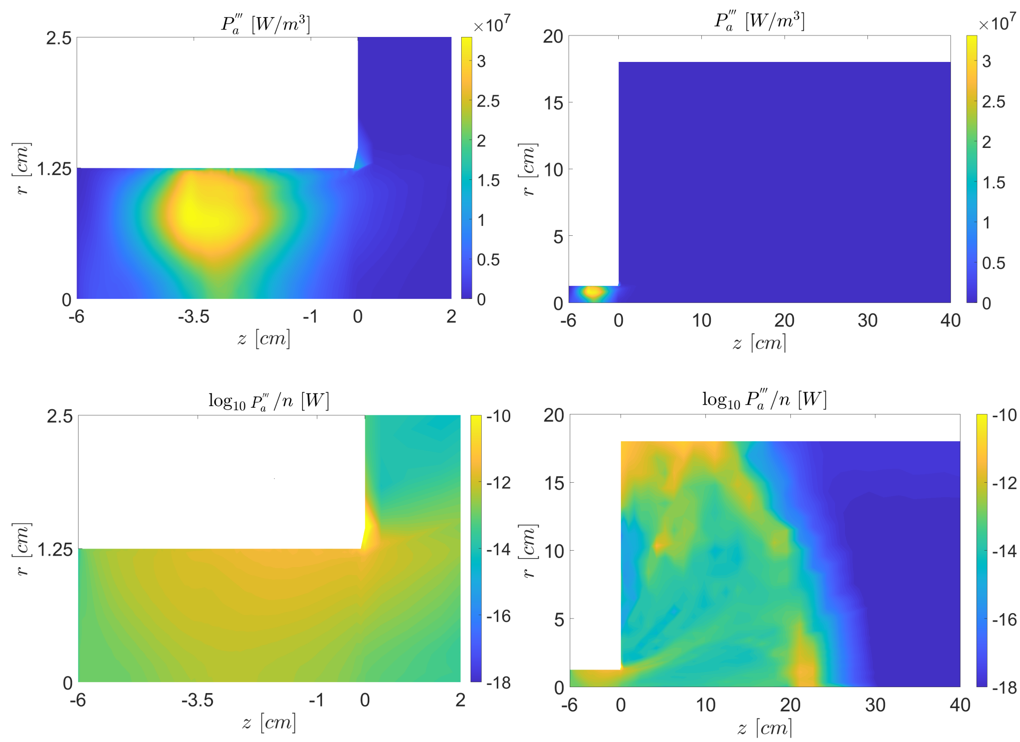

Fig. 10 Electromagnetic Power Deposition (top row), power per electron (bottom). Zooms at the source region (left column) and full transport domain (right column).

electron heating. The per-particle absorption can be observed to peak inside the source and at the ECR resonance, revealing the importance of power deposition in this region of the plume. While earlier works have relied on computing the absorption only inside the source [36], these results suggest that the local heating can change substantially the structure of the plume and drive the electron temperature profile outside of the source, as shown in figure 5, clearly observable in the plume periphery.

D. Performance figures

From the results above, we can compute several performance figures that help understand the main drivers of inefficiencies in the device.

Of the total mass flow of neutral gas injected into the source, only a fraction will leave the domain as ions, $\dot{m}_{iP}$, while the remaining will just not be ionized or will recombine. The utilization efficiency is defined as

$$\eta_u = \frac{\dot{m}_{i,beam}}{\dot{m}}. \tag{25}$$

The ion volumetric production $\dot{m}_{i,total}$ must either leave the domain or be collected on the dielectric walls inside the source. The former fraction of ions is the only one useful for the generation of thrust. Accordingly, we can define the production efficiency as the ratio of the beam ion mass flow to the total volumetric production

$$\eta_{prod} = \frac{\dot{m}_{i,beam}}{\dot{m}_{i,total}} \tag{26}$$

where the mass flows are the sum for all ion species. The mass flow to the dielectric walls $\dot{m}_{i,wall} = \dot{m}_{i,total} - \dot{m}_{i,beam}$ is recombined back into neutrals.

In the present simulation, $\eta_u \approx 64\%$ and $\eta_{prod} \approx 9\%$. These figures, rather than indicating that ionization is inefficient, highlight the enormous losses to the dielectric walls. Considering the ratio between the two, a neutral can be estimated to suffer 6 ionization processes on average before leaving the source. This number is similar to other observations in a HPT with a similar vessel dimensions but with a different magnetic topology [14].

The total power balance can be split into the fraction of kinetic power leaving through free loss surface with the plume, the kinetic losses to walls, and an extra term accounting for inelastic collisional processes (excitation and ionization collisions) $P_a = P_{beam} + P_{wall} + P_{inel}$. Indeed, excitation collisions represent a loss of power, since excited atoms/ions eventually decay back to their ground state emitting a photon, which is conservatively assumed lost from the system. Respectively, ionization energy is considered a loss upon ion creation, and it is not counted again as wall losses when ions recombine at the walls. The energy efficiency is defined as:

$$\eta_{ene} = P_{beam}/P_a. \tag{27}$$

Analyzing further the loss factors ϵ_{wall} and ϵ_{inel}, i.e. the fraction of total power that is lost at the walls and inelastic processes respectively, we see that about 94% of the kinetic power to dielectrics occurs at the lateral source wall. The difference on the power flux between the back and lateral walls is not only explained by the greater area of the later, but also by the presence of the separatrix where the magnetic lines direct the plasma from the axis towards the wall (see Figure 7). Regarding the inelastic losses, the most noticeable fact is the enormous power wasted in excitation of neutral Xe. About 68% of ϵ_{inel} is attributed to this process alone. The rest goes to ionization, with only a minor contribution to double ionization.

The kinetic wall and inelastic losses are fundamentally coupled. The large fluxes to the walls and the resulting new neutrals prevent an efficient temperature rise inside the source which, in turn, leads to high inelastic losses due to excitation, the dominant inelastic process at low T_e.

Regarding P_{beam}, not all the kinetic beam power is available for thrust. The divergence efficiency assesses which fraction of the plasma (i.e. ion plus electron) energy is axial, and the dispersion efficiency quantifies the level of velocity dispersion of all species. This last figure would be exactly one for a fully monoenergetic plasma:

$$\eta_{div} = \frac{P_{beam}^{(z)}}{P_{beam}}, \quad \eta_{disp} = \frac{F^2}{2\dot{m}P_{beam}^{(z)}} \tag{28}$$

where F is the thrust force. The divergence efficiency $\eta_{div} \approx 47\%$ is significantly low compared to other EPT simulations and laboratory measurements. This is attributed to the magnetic topology and rapidly closing lines. Introducing these two last performance figures, the total propulsion or thrust efficiency can be computed as

$$\eta_F = \eta_{ene}\eta_{div}\eta_{disp} = \frac{F^2}{2\dot{m}P_a}. \tag{29}$$

A summary of the efficiencies and loss factors discussed above can be found in Table 3.

Thrust (mN)	η_F	η_{div}	η_u	η_{prod}	η_{disp}	η_{ene}	ϵ_{wall}	ϵ_{inel}
5.1	0.026	0.47	0.64	0.09	0.57	0.10	0.33	0.57

Table 3 Thrust and propulsive performances

IV. Conclusion

The self-consistent discharge of a Helicon Plasma Thruster has been modelled, simulated and analyzed coupling a transport and a wave code. Advances in the transport side of the problem include the utilization of a larger domain, low density plume regions and new downstream boundary conditions. The HYPHEN hybrid solver has also been shown capable of dealing with a complex magnetic topology, which includes singular points, and highly turning magnetic field lines (challenging for the magnetically aligned mesh MFAM).

Regarding the wave solver, a new Finite Element Frequency Domain (FEFD) code has been employed. When compared to the previous finite difference solver [11] we observe a gain in speed and accuracy. In particular, the conforming element discretization shows an enhanced behavior across transitions, notably at the under-dense to over-dense limit $P = 0$. Additionally, compared to other FEM tools developed in the past for the study of the plasma-wave interaction in electrodeless thrusters [19], the algorithm employed in this work includes a Fourier expansion of azimuthal (out-of-plane) fields that is indispensable for the study of axisymmetric Helicon thrusters with 3D antennas.

The wave and transport enhancements have allowed a self-consistent 2D discharge study of the HPT03, which features a magnetic ring cusp inside the source.

Transport results indicate high wall losses driven mainly by the non-axial magnetic topology at the source; large amounts of energy wasted in inelastic excitation of neutrals, a behavior related to the low temperature of the plasma and coupled to the high wall losses; and a high plume divergence, once more attributable to the magnetic topology.

Moreover, the large computational domain has enabled the simulation of the Electron Cyclotron Resonance surface that is always downstream. Being far away from the plasma source the ECR has been traditionally ignored in coupled simulations with most approximations only modelling the heating inside the source [30, 36]. We have shown that, despite almost all the electromagnetic power being deposited at the source, the power per electron peaks at the ECR and that this aspect determines the electron temperature map in the plume. Future work and comparison between the source-only heating and global heating simulations is needed to confirm this hypothesis.

Future work must also include parametric studies with varying singular point and antenna positions.

Acknowledgments

The authors would also like to thank Jaume Navarro for his inputs on the prototype design and laboratory measurements. This work has been supported by the HIPATIA project, funded by the European Union's Horizon 2020 Research and Innovation Program, under Grant Agreement number 870542.

References

[1] Takahashi, K., Charles, C., Boswell, R., and Ando, A., "Performance improvement of a permanent magnet helicon plasma thruster," *Journal of Physics D: Applied Physics*, Vol. 46, No. 35, 2013, p. 352001.

[2] Shinohara, S., Nishida, H., Tanikawa, T., Hada, T., Funaki, I., and Shamrai, K. P., "Development of electrodeless plasma thrusters with high-density helicon plasma sources," *IEEE Transactions on Plasma Science*, Vol. 42, No. 5, 2014, pp. 1245–1254.

[3] Trezzolani, F., Lucca Fabris, A., Pavarin, D., et al., "Low power radio-frequency plasma thruster developement and testing," *33th International Electric Propulsion Conference*, 2013.

[4] Navarro-Cavallé, J., Wijnen, M., Fajardo, P., and Ahedo, E., "Experimental characterization of a 1 kW helicon plasma thruster," *Vacuum*, Vol. 149, 2018, pp. 69–73.

[5] Chen, G., and Raja, L. L., "Fluid modeling of electron heating in low-pressure, high-frequency capacitively coupled plasma discharges," *Journal of applied physics*, Vol. 96, No. 11, 2004, pp. 6073–6081.

[6] Bose, D., Govindan, T., and Meyyappan, M., "Modeling of a Helicon Plasma Source," *IEEE Transactions on Plasma Science*, Vol. 31, 2003, pp. 464–470.

[7] Magarotto, M., Melazzi, D., and Pavarin, D., "3D-VIRTUS: Equilibrium condition solver of radio-frequency magnetized plasma discharges for space applications," *Computer Physics Communications*, Vol. 247, 2020, p. 106953.

[8] Zhou, J., Pérez-Grande, D., Fajardo, P., and Ahedo, E., "Numerical treatment of a magnetized electron fluid within an electromagnetic plasma thruster code," *Plasma Sources Science and Technology*, Vol. 28, No. 11, 2019, p. 115004.

[9] Melazzi, D., and Lancellotti, V., "ADAMANT: A surface and volume integral-equation solver for the analysis and design of helicon plasma sources," *Computer Physics Communications*, Vol. 185, No. 7, 2014, pp. 1914–1925.

[10] Jiménez, P., Merino, M., and Ahedo, E., "Preliminary investigation of the electromagnetic fields in the far plume of a Helicon Plasma Thruster," *Space Propulsion Conference 2021*, Association Aéronautique et Astronautique de France, 2021.

[11] Jiménez, P., Merino, M., and Ahedo, E., "Wave propagation and absorption in a Helicon plasma thruster source and its plume," *Plasma Sources Science and Technology*, Vol. 31, No. 4, 2022, p. 045009. https://doi.org/10.1088/1361-6595/ac5ecd, URL https://doi.org/10.1088/1361-6595/ac5ecd.

[12] Fife, J. M., "Hybrid-PIC modeling and electrostatic probe survey of Hall thrusters," Ph.D. thesis, Massachusetts Institute of Technology, 1998.

[13] Cichocki, F., Merino, M., Ahedo, E., Smirnova, M., Mingo, A., and Dobkevicius, M., "Electric Propulsion Subsystem Optimization for "Ion Beam Shepherd" Missions," *Journal of Propulsion and Power*, Vol. 33, No. 2, 2017, pp. 370–378. https://doi.org/10.2514/1.B36105.

[14] Zhou, A., J. Domínguez-Vazquez, Fajardo, P., and Ahedo, E., "Magnetized fluid electron model within a two-dimensional hybrid simulation code for electrodeless plasma thrusters," *Plasma Sources Science and Technology*, Vol. 31, No. 4, 2022, p. 045021.

[15] Hepner, S., and Jorns, B., "The role of low frequency drift waves in driving non-classical transport in magnetic nozzles," *AIAA Propulsion and Energy 2020 Forum*, 2020, p. 3644.

[16] Parra, F. I., Ahedo, E., Fife, J. M., and Martínez-Sánchez, M., "A two-dimensional hybrid model of the Hall thruster discharge," *Journal of Applied Physics*, Vol. 100, No. 2, 2006, p. 023304.

[17] Domínguez-Vázquez, A., "Axisymmetric simulation codes for Hall effect thrusters and plasma plumes," Ph.D. thesis, Universidad Carlos III de Madrid, Leganés, Spain, 2019.

[18] Domínguez-Vázquez, A., Zhou, J., Sevillano-González, A., Fajardo, P., and Ahedo, E., "Analysis of the electron downstream boundary conditions in a 2D hybrid code for Hall thrusters," 37^{th} *International Electric Propulsion Conference*, Electric Rocket Propulsion Society, Boston, MA, June 19-23, 2022.

[19] Sánchez-Villar, A., Zhou, J., Merino, M., and Ahedo, E., "Coupled plasma transport and electromagnetic wave simulation of an ECR thruster," *Plasma Sources Science and Technology*, Vol. 30, No. 4, 2021, p. 045005. https://doi.org/10.1088/1361-6595/abde20.

[20] Jin, J.-M., and Riley, D. J., *Finite element analysis of antennas and arrays*, John Wiley & Sons, 2009.

[21] Chen, G., Arefiev, A., Bengtson, R., Breizman, B., Lee, C., and Raja, L., "Resonant power absorption in helicon plasma sources," *Physics of Plasmas*, Vol. 13, 2006, p. 123507.

[22] Stix, T. H., *Waves in plasmas*, Springer Science & Business Media, 1992.

[23] Monk, P., *Finite element methods for Maxwell's equations*, Oxford University Press, 2003.

[24] Nédélec, J.-C., "Mixed finite elements in $\mathbb{R}^3$," *Numerische Mathematik*, Vol. 35, No. 3, 1980, pp. 315–341.

[25] Kamenski, I., and Borg, G., "An evaluation of different antenna designs for helicon wave excitation in a cylindrical plasma source," *Physics of Plasmas*, Vol. 3, 1996, p. 4396.

[26] Tian, B., Merino, M., and Ahedo, E., "Two-dimensional plasma-wave interaction in an helicon plasma thruster with magnetic nozzle," *Plasma Sources Science and Technology*, Vol. 27, No. 11, 2018, p. 114003.

[27] Tian, B., "Modeling of physical processes in radio-frequency plasma thrusters," Ph.D. thesis, 2017.

[28] Chen, F., "The low-field density peak in helicon discharges," *Physics of Plasmas*, Vol. 10, 2003, p. 2586.

[29] Gómez, V., Gimńez, A., Ruiz, M., Navarro-Cavallé, J., Fajardo, P., Wijnen, M., and Ahedo, E., "RF power-plasma coupling experimental results in a helicon plasma thruster prototype," 36^{th} *International Electric Propulsion Conference*, Electric Rocket Propulsion Society, Vienna, Austria, 2019.

[30] Zhou, J., Jiménez, P., Merino, M., Fajardo, P., and Ahedo, E., "Numerical Simulations of the Plasma Discharge in a Helicon Plasma Thruster," 36^{th} *International Electric Propulsion Conference*, Electric Rocket Propulsion Society, Vienna, Austria, 2019.

[31] Little, J., and Choueiri, E., "Electron Cooling in a Magnetically Expanding Plasma," *Physical Review Letters*, Vol. 117, No. 22, 2016, p. 225003.

[32] Zhang, Y., Charles, C., and Boswell, R., "Thermodynamic study on plasma expansion along a divergent magnetic field," *Physical review letters*, Vol. 116, No. 2, 2016, p. 025001.

[33] Zhou, J., Sánchez-Arriaga, G., and Ahedo, E., "Time-dependent expansion of a weakly-collisional plasma beam in a paraxial magnetic nozzle," *Plasma Sources Science and Technology*, Vol. 30, No. 4, 2021, p. 045009. https://doi.org/10.1088/1361-6595/abeff3.

[34] Merino, M., Nuez, J., and Ahedo, E., "Fluid-kinetic model of a propulsive magnetic nozzle," *Plasma Sources Science and Technology*, Vol. 30, No. 11, 2021, p. 115006. https://doi.org/10.1088/1361-6595/ac2a0b, URL https://doi.org/10.1088/1361-6595/ac2a0b.

[35] Blackwell, D., Madziwa, T., Arnush, D., and Chen, F., "Evidence for Trivelpiece-Gould modes in a helicon discharge," *Physical review letters*, Vol. 88, No. 14, 2002, p. 145002.

[36] Souhair, N., Magarotto, M., Majorana, E., Ponti, F., and Pavarin, D., "Development of a lumping methodology for the analysis of the excited states in plasma discharges operated with argon, neon, krypton, and xenon," *Physics of Plasmas*, Vol. 28, No. 9, 2021, p. 093504.